

# Solution for null field CVBIE in plane elasticity using an accurate shape function

Y.Z. Chen\*

*Division of Engineering Mechanics, Jiangsu University, Zhenjiang, Jiangsu, 212013  
People's Republic of China*

*(Received January 6, 2019, Revised June 8, 2019, Accepted December 27, 2020)*

**Abstract.** This paper provides a numerical solution for null field complex variable boundary integral equation (CVBIE) in plane elasticity. All kernels in the null field CVBIE are regular function. An accurate shape function for the displacement and traction along the contour is suggested. With the usage of suggested shape function, a discretization for the boundary integral equation (BIE) is carried out. The Dirichlet and the Neumann boundary value problems (BVPs) for the interior region and the exterior region are studied. Two numerical examples are provided in the paper. It is shown that a higher accuracy has been achieved in the examples with the usage of the suggested shape function.

**Keywords:** null field formulation; complex variable boundary integral equation; interior BVP; exterior BVP; accurate shape function

---

## 1. Introduction

In recent sixty years, the boundary integral equation method (BIE) becomes an important tool in the solution of elasticity problem. Many pioneer researchers initiated and developed the general theorem in the field of BIE (Rizzo 1967, Cruse 1969, Jaswon and Symm 1977, Brebbia *et al.* 1984, Hong and Chen 1988). The usual BIE is formulated on the usage of the Betti's reciprocal theorem between the fundamental stress field and the physical field. For the general case of boundary and the boundary condition, the formulated BIE cannot be solved in a closed form. After making a discretization to the BIE, it is natural to formulate the boundary element method (BEM). The heritage and history for the BIE were summarized (Cheng and Cheng 2005). The BEM has a particular feature that the relevant numerical discretization is conducted at reduced spatial dimension. Generally, the reduced dimension leads to smaller linear systems and less computer memory requirements.

However, the BIE for plane elasticity problem suffers some inconvenient points. For example, in the Dirichlet problem for the exterior boundary value problem (BVP), the solution from BIE may not be unique in the case of degenerate scale for contour configuration. There are extensive references in the field of degenerate scales (Chen *et al.* 2002, Vodicka and Mantic 2008). Clearly,

---

\*Corresponding author, Professor, E-mail: [chens@ujs.edu.cn](mailto:chens@ujs.edu.cn)

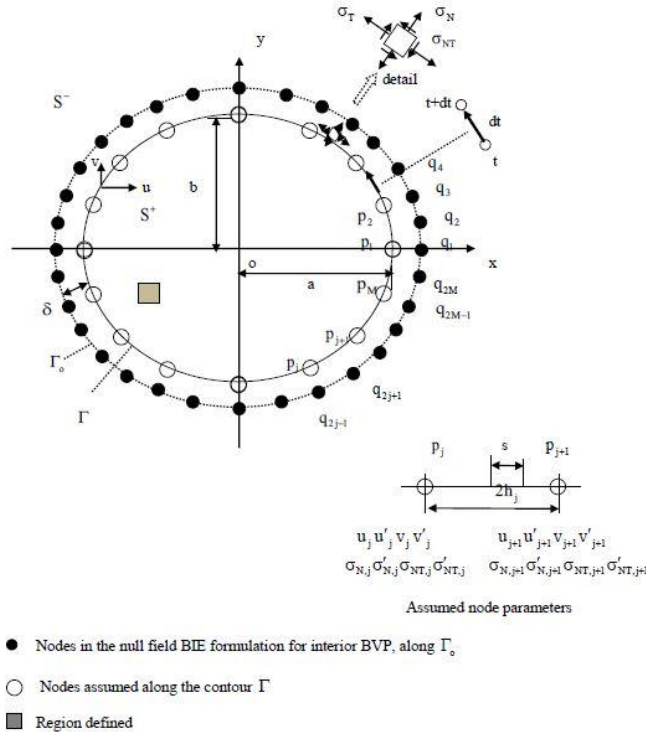


Fig. 1 Formulation of the null field CVBIE for an interior region

the physical background for the presence of degenerate scale in plane elasticity is rather clear.

Secondly, there are some singular or super singular integrals involved in the BIE. Sometimes, it may be a problem to evaluate those integrals properly. To avoid using the singular integral in BIE many researchers suggested the regularization procedure for BIE or the no-singular boundary element formulation (Liu and Rudolphi 1999, Liu and Deng 2013).

The other possibility in the regularization procedure is based on the usage of to the null field formulation for the usual BIE. Some solutions in the Laplace equation based on the null field formulation were suggested more recently (Chen and Wu 2007, Chen and Lee 2009). In those papers, the kernels and the functions assumed along the boundary are expressed in the series form. Further, the discretization for the BIE is suggested.

An exact solution was proposed for the hypersingular boundary integral equation of two-dimensional elastostatics (Zhang and Zhang 2008). Based on complex variable boundary integral equation, an iteration approach for multiple notch problem was suggested (Chen 2012b). Properties of integral operators in complex variable boundary integral equation in plane elasticity were studied in detail (Chen and Wang 2013).

This paper provides a numerical solution for null field complex variable boundary integral equation (CVBIE) in plane elasticity. This null field CVBIE can be easily formulated from relevant CVBIE obtained previously (Chen *et al.* 2010, Chen 2012a). The interior and exterior boundary value problems (BVPs) are studied in the present paper. Since all source points are located in the complementary domain with respect to the considered domain, all kernels in the null field BIE are regular function. An accurate shape function for displacement and traction along the

contour is suggested in the paper. For each node on the contour two values are assumed, one is the value of the function itself on the node and the other is the derivative for the function. The shape function is therefore formulated on many intervals along the contour. Therefore, the assumed shape function has the property of  $C^1$  continuity. The elliptic contour is assumed in the numerical examples. Comparisons between the exact solution and the numerical solution for the Dirichlet and the Neumann problems are carried out. In the present examples, all the relative errors in both the Dirichlet and the Neumann problems are very small.

## 2. The Null Field CVBIE for an interior region in plane elasticity

General formulation for the null field CVBIE for an interior region is suggested. An accurate shape function for modeling the displacement and traction along the contour is proposed in the discretization of BIE. Numerical examples are carried out.

### 2.1 General formulation for the null field CVBIE for an interior region

In the following analysis, we take the elliptic contour as an example in the formulation (Fig. 1). Previously, a CVBIE (complex variable boundary integral equation) for the interior region was suggested (Chen *et al.* 2010, Chen 2012a). After dropping the free term in the usual CVBIE, and assuming the source point  $t_0$  to be outside the contour  $\Gamma$  or  $t_0 \in S^-$  (Fig. 1), we have the following null field CVBIE for the interior BVP (boundary value problem).

$$\begin{aligned} & 2G \int_{\Gamma} \left( \frac{\kappa-1}{t-t_0} U(t) dt - L_1(t, t_0) U(t) dt + L_2(t, t_0) \overline{U(t)} dt \right) \\ & = \int_{\Gamma} \left( 2\kappa \ln |t-t_0| Q(t) dt + \frac{t-t_0}{\bar{t}-\bar{t}_0} \overline{Q(t)} d\bar{t} \right), \quad (t_0 \in S^-, \text{ for interior BVP}) \end{aligned} \quad (1)$$

where  $\kappa = 3-4\nu$  (for plane strain condition),  $\kappa = (3-\nu)/(1+\nu)$  (for plane stress condition),  $G$  is the shear modulus of elasticity, and  $\nu$  is the Poisson's ratio. In Eq. (1),  $\Gamma$  denotes the boundary of the interior region. The integration for "dt" is performed in the clock-wise direction in Fig. 1. In addition,  $U(t)$  and  $Q(t)$  denote the displacement and traction along the boundary, which are defined by

$$U(t) = u(t) + iv(t), \quad Q(t) = \sigma_N(t) + i\sigma_{NT}(t), \quad (t \in \Gamma) \quad (2)$$

In addition, two kernels are defined by (Chen *et al.* 2010, Chen 2012a)

$$\begin{aligned} L_1(t, \tau) &= -\frac{d}{dt} \left\{ \ln \frac{t-\tau}{\bar{t}-\bar{\tau}} \right\} = -\frac{1}{t-\tau} + \frac{1}{\bar{t}-\bar{\tau}} \frac{d\bar{t}}{dt} \\ L_2(t, \tau) &= \frac{d}{dt} \left\{ \frac{t-\tau}{\bar{t}-\bar{\tau}} \right\} = \frac{1}{\bar{t}-\bar{\tau}} - \frac{t-\tau}{(\bar{t}-\bar{\tau})^2} \frac{d\bar{t}}{dt} \end{aligned} \quad (3)$$

Note that all the nodes for the null field BIE, or the points  $t_0$  are located outside of the contour  $\Gamma$

Thus, all integrals involved in Eq. (1) are regular. The ellipse for null field nodes  $t_0$  is defined by,  $x=(a+\delta)\cos\theta$ ,  $y=(b+\delta)\sin\theta$  or  $t_0 \in \Gamma_0$  (Fig. 1).

## 2.2 Discretization in the Null field BIE for the interior BVP

It is known that it is an import step to perform discretization in the numerical solution of BIE. An ellipse with two half-axes “a” and “b” is taken as an example in the discretization (Fig. 1). In the discretization, we can assume N nodes, from  $P_1, P_2, P_j, P_{j+1}, P_M$  along the contour  $\Gamma$  (Fig. 1). Clearly, the node  $P_j$  corresponds to a location with the coordinates  $x=a\cos\{2(j-1)\pi/M\}$  and  $y=b\sin\{2(j-1)\pi/M\}$  ( $j=1,2,\dots,M$ ).

In the discretization, the parameter  $\theta$  in the expression for the elliptic contour  $\Gamma$ , or  $x=-a\cos\theta$  and  $y=b\sin\theta$ , is appropriate one in the derivation. Here we prefer write the parameter “ $\theta$ ” as “s” (Fig. 1).

For the u-component of the displacement (the real portion of  $U=u+iv$ ) along the interval  $P_jP_{j+1}$  (Fig. 1), we can assume the shape function for the displacement as follows

$$u^{(j)}(s) = g_1 + g_2 \left( \frac{s}{h_j} \right) + g_3 \left( \frac{s}{h_j} \right)^2 + g_4 \left( \frac{s}{h_j} \right)^3, \quad |s| \leq h_j \quad (4)$$

$$h_j \frac{du^{(j)}(s)}{ds} = g_2 + 2g_3 \left( \frac{s}{h_j} \right) + 3g_4 \left( \frac{s}{h_j} \right)^2, \quad |s| \leq h_j \quad (5)$$

where  $h_j = \pi/M$  denotes the half-length in the integration for the interval  $P_jP_{j+1}$  (Fig. 1).

For the four undetermined coefficients  $g_i$  ( $i=1,2,3,4$ ) in the shape function  $u^{(j)}(s)$ , we can propose the following conditions

$$u^{(j)}(s) \Big|_{s=-h_j} = u_j, \quad \frac{du^{(j)}(s)}{ds} \Big|_{s=-h_j} = u'_j, \quad u^{(j)}(s) \Big|_{s=h_j} = u_{j+1}, \quad \frac{du^{(j)}(s)}{ds} \Big|_{s=h_j} = u'_{j+1} \quad (6)$$

From the condition shown by Eq. (6), we can obtain the following interpolation for the shape function  $u^{(j)}(s)$

$$\begin{aligned} u^{(j)}(s) = & u_j \left( \frac{1}{2} - \frac{3}{4} \left( \frac{s}{h_j} \right) + \frac{1}{4} \left( \frac{s}{h_j} \right)^3 \right) + u'_j \left( \frac{1}{4} - \frac{1}{4} \left( \frac{s}{h_j} \right) - \frac{1}{4} \left( \frac{s}{h_j} \right)^2 + \frac{1}{4} \left( \frac{s}{h_j} \right)^3 \right) h_j \\ & + u_{j+1} \left( \frac{1}{2} + \frac{3}{4} \left( \frac{s}{h_j} \right) - \frac{1}{4} \left( \frac{s}{h_j} \right)^3 \right) + u'_{j+1} \left( -\frac{1}{4} - \frac{1}{4} \left( \frac{s}{h_j} \right) + \frac{1}{4} \left( \frac{s}{h_j} \right)^2 + \frac{1}{4} \left( \frac{s}{h_j} \right)^3 \right) h_j \end{aligned} \quad (7)$$

Similarly, for the v-component of the displacement (the imaginary portion of  $U=u+iv$ ) along the interval  $P_jP_{j+1}$ , we have the following interpolation for the shape function  $v^{(j)}(s)$

$$\begin{aligned}
& + v_{j+1} \left( \frac{1}{2} + \frac{3}{4} \left( \frac{s}{h_j} \right) - \frac{1}{4} \left( \frac{s}{h_j} \right)^3 \right) + v'_{j+1} \left( -\frac{1}{4} - \frac{1}{4} \left( \frac{s}{h_j} \right) + \frac{1}{4} \left( \frac{s}{h_j} \right)^2 + \frac{1}{4} \left( \frac{s}{h_j} \right)^3 \right) h_j, \quad |s| < h_j \\
& + v_{j+1} \left( \frac{1}{2} + \frac{3}{4} \left( \frac{s}{h_j} \right) - \frac{1}{4} \left( \frac{s}{h_j} \right)^3 \right) + v'_{j+1} \left( -\frac{1}{4} - \frac{1}{4} \left( \frac{s}{h_j} \right) + \frac{1}{4} \left( \frac{s}{h_j} \right)^2 + \frac{1}{4} \left( \frac{s}{h_j} \right)^3 \right) h_j, \quad |s| < h_j
\end{aligned} \tag{8}$$

where

$$v^{(j)}(s) \Big|_{s=-h_j} = v_j, \quad \frac{dv^{(j)}(s)}{ds} \Big|_{s=-h_j} = v'_j, \quad v^{(j)}(s) \Big|_{s=h_j} = v_{j+1}, \quad \frac{dv^{(j)}(s)}{ds} \Big|_{s=h_j} = v'_{j+1} \tag{9}$$

Note that the two shape functions  $u^{(j)}(s)$  and  $v^{(j)}(s)$  are defined in the local coordinates with origin at the middle point of the interval  $p_j p_{j+1}$  (Fig. 1). However, it is easy to link the position of “s” to the position of “t” in the term  $L_1(t, t_0)U(t)$  in BIE shown by Eq. (1). In addition, the two shape functions  $u^{(j)}(s)$  and  $v^{(j)}(s)$  have the property of the  $C^1$  continuity. The same interpolation for the traction components  $\sigma_N^{(j)}(s)$  and  $\sigma_{NT}^{(j)}(s)$  is used in the discretization.

In order to balance the members of the equations and unknowns after discretization, we assume the  $2M$  null field nodes for the source point  $t_0$  in Eq. (1) (Fig. 1). Those null field nodes are denoted by  $q_1, q_2, q_3, q_4, \dots, q_{2j-1}, q_{2j}, q_{2j+1}, q_{2j+2}, \dots, q_{2M-1}, q_{2M}$ . In addition, those points are assumed on an ellipse which is defined by  $x = (a + \delta) \cos \theta$  and  $y = (b + \delta) \sin \theta$ . Clearly, the ellipse for the null field nodes  $\Gamma_0$  is located exterior to the contour  $\Gamma$  (Fig. 1).

If we assume the source point  $t_0$  in the points from  $q_1, q_2, \dots$  to  $q_{2M-1}, q_{2M}$ , we will obtain  $2M$  equations in complex variable, or  $4M$  equations in real.

Simply substituting the assumed shape function for  $U(t) = u(t) + iv(t)$  and  $Q(t) = \sigma_N(t) + i\sigma_{NT}(t)$  into Eq. (1) and performing the integration, the BIE shown by Eq. (1) can be reduced to the following the following form of linear algebraic equation

$$\mathbf{M}_U \{U(t)\} = \mathbf{M}_Q \{Q(t)\} \quad (t \text{ denoting the discrete points}) \tag{10}$$

where

$$\{U(t)\} = \{u_1 u'_1 v_1 v'_1 \dots u_j u'_j v_j v'_j \dots u_M u'_M v_M v'_M\}^T \tag{11}$$

$$\{Q(t)\} = \{\sigma_{N,1} \sigma'_{N,1} \sigma_{NT,1} \sigma'_{NT,1} \dots \sigma_{N,j} \sigma'_{N,j} \sigma_{NT,j} \sigma'_{NT,j} \dots \sigma_{N,M} \sigma'_{N,M} \sigma_{NT,M} \sigma'_{NT,M}\}^T \tag{12}$$

As stated previously,  $\sigma_{N,j} \sigma'_{N,j} \sigma_{NT,j} \sigma'_{NT,j}$  denote the value of  $\sigma_N$ ,  $d\sigma_N/ds$ ,  $\sigma_{NT}$ ,  $d\sigma_{NT}/ds$  at the node  $p_j$ , respectively. In Eqs. (11) and (12), both vectors  $\{U(t)\}$  and  $\{Q(t)\}$  have the dimension  $4M \times 1$ .

In Eq. (10), the matrix  $\mathbf{M}_U$  is called the matrix acting upon the displacement vector  $\{U(t)\}$ ,

and  $\mathbf{M}_Q$  the matrix acting upon the traction vector  $\{Q(t)\}$ . Both matrices  $\mathbf{M}_U$  and  $\mathbf{M}_Q$  have the dimension.  $4M \times 4M$ .

In the Dirichlet BVP, the vector  $\{U(t)\}$  is given beforehand. Substituting the known vector  $\{U(t)\}$  into Eq. (10), the equation will be reduced to a linear algebraic equation for the traction  $\{Q(t)\}$ . Similarly, in the Neumann BVP, the vector  $\{Q(t)\}$  is given beforehand. Substituting the known vector  $\{Q(t)\}$  into Eq. (10), the equation will be reduced to a linear algebraic equation for the displacement  $\{U(t)\}$ .

### 2.3 Numerical example

One numerical example is presented below to prove the effectiveness of the proposed scheme for computation. The elastic elliptic region with two half-axes “a” and “b” is used for the numerical examination (Fig. 1). In computation,  $M=48$  divisions is used for the elliptic contour  $\Gamma$ . The ellipse for null field nodes  $t_o$  is defined by  $x = (a + \delta)\cos\theta$ ,  $y = (b + \delta)\sin\theta$ . or  $t_o \in \Gamma_o$  and  $\delta=0.02a$  is used in computation (Fig. 1). When we perform the integration along the interval, for example along  $p_j p_{j+1}$ , the Simpson integration rule with 60 divisions is used (Hildebrand 1974).

In the examination, we use the following complex potentials (Muskhelishvili 1953)

$$\phi(z) = c_1 \frac{z^2}{a} p, \psi(z) = c_2 \frac{z^2}{a} p \quad (13)$$

where “p” is a loading and  $c_i$  ( $i=1,2$ ) are some complex constants.

From Eq. (13), we can evaluate the relevant displacements and stresses by using the Appendix A. In fact, the displacement and stress states in the region and boundary will be fully determined by the assumed coefficients  $c_i$  ( $i=1,2$ ).

In the example, we choose  $c_1 = 0.5 + 0.8i$ ,  $c_2 = 1.1 + 0.6i$ , and  $b/a=0.5$ . In addition, we choose  $a=20$ ,  $b=10$  and  $G=2$  in computation

As mentioned above, after discretization to Eq. (1), the BIE can be written in the form

$$\mathbf{M}_U \{U(t)\} = \mathbf{M}_Q \{Q(t)\} \quad (t \text{ denoting the discrete points}) \quad (14)$$

where  $\mathbf{M}_U$  a matrix acting upon the displacement vector  $\{U(t)\}$ , and  $\mathbf{M}_Q$  is a matrix acting upon the traction vector  $\{Q(t)\}$ .

In the examination,  $\{U_{ex}(t)\}$  and  $\{Q_{ex}(t)\}$  denotes the displacement and traction vectors obtained from the exact solution with the complex potentials shown by Eq. (13) and some expressions for plane elasticity in Appendix A.

In the first examination, we examine the properties of matrices  $\mathbf{M}_U$  and  $\mathbf{M}_Q$ . From assumed two vectors  $\{U_{ex}(t)\}$  and  $\{Q_{ex}(t)\}$ , we can formulate and evaluate the following two vectors

$$\{U_p(t_o)\} = \mathbf{M}_U \{U_{ex}(t)\}, \quad (t_o \in \Gamma_o) \quad (15)$$

$$\{Q_p(t_o)\} = M_Q \{Q_{ex}(t)\}, \quad (t_o \in \Gamma_o) \quad (16)$$

From Eqs. (14), (15), (16), we see that  $\{U_p(t_o)\} \approx \{Q_p(t_o)\}$ . Thus, the approximation of the vector  $\{U_p(t_o)\}$  to the vector  $\{Q_p(t_o)\}$  represents the accuracy achieved in computation. Note that many null field points  $t_o \in \Gamma_o$  are located at the null field nodes  $q_1, q_2, \dots, q_{2M-1}, q_{2M}$  (Fig. 1).

Thus, we can define a vector

$$\{e_1(t_o)\} = \{U_p(t_o)\} - \{Q_p(t_o)\} = M_U \{U_{ex}(t)\} - M_Q \{Q_{ex}(t)\} \quad (t_o \in \Gamma_o) \quad (17)$$

and define an error estimation value

$$E_{r1} = \frac{\max |\{e_1(t_o)\}|}{\max \text{ of } |M_U \{U_{ex}(t_o)\}| \text{ and } |M_Q \{Q_{ex}(t_o)\}|} \quad (18)$$

After computation, we find the following error  $E_{r1} = 0.867 * 10^{-4}$  from  $2M$  discrete points.

Clearly, the error is very small.

In the second examination, we study the Dirichlet problem. In the Dirichlet problem, the  $U(t)$  component denoted by  $\{U_{ex}(t)\}$  can be exactly evaluated beforehand, which is from the complex

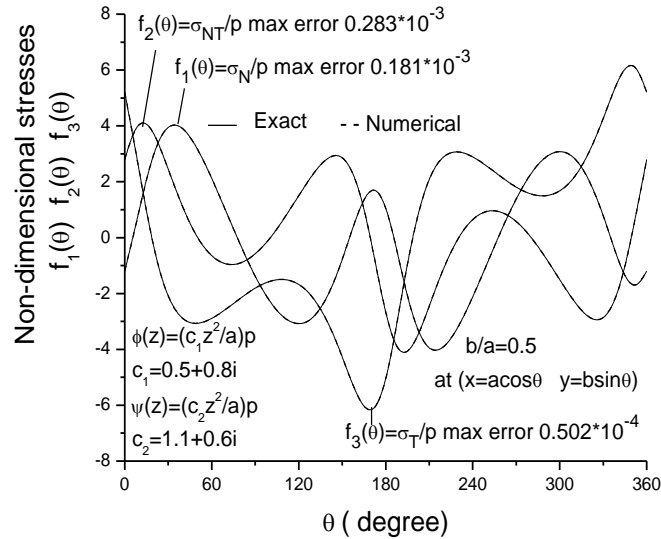


Fig. 2 Comparisons for three non-dimensional stresses  $f_1(\theta) = \sigma_N / p$ ,  $f_2(\theta) = \sigma_{NT} / p$  and  $f_3(\theta) = \sigma_T / p$  in a Dirichlet problem for an elliptic plate in the case of  $c_1 = 0.5 + 0.8i$ ,  $c_2 = 1.1 + 0.6i$ , and  $b/a=05$  (see Fig. 1, Eq. (13) and Appendix A)

potentials shown by Eq. (13) with  $c_1 = 0.5 + 0.8i$  and  $c_2 = 1.1 + 0.6i$  directly. Thus, from Eq. (14), we can get the solution for  $\{Q_{\text{num}}(t)\}$  by

$$\{Q_{\text{num}}(t)\} = \mathbf{M}_Q^{-1} \mathbf{M}_U \{U_{\text{ex}}(t)\}, \quad (t \text{ denoting the discrete points}) \quad (19)$$

where  $\mathbf{M}_Q^{-1}$  denotes the inverse of the matrix  $\mathbf{M}_Q$ . Here, we only consider the elliptic region with  $a=20$  and  $b=10$ . Thus, the inverse matrix  $\mathbf{M}_Q^{-1}$  exists when the real scale is different to the degenerate scale.

From the obtained vector  $\{Q_{\text{num}}(t)\}$  from numerical solution, we can get the traction components  $\sigma_{N,\text{num}}(t), \sigma_{NT,\text{num}}(t)$  at many discrete points along the boundary. Those values are compared with  $\sigma_{N,\text{ex}}(t), \sigma_{NT,\text{ex}}(t)$ . Finally, we find the following errors:  $\max |\sigma_{N,\text{num}}(t_j) - \sigma_{N,\text{ex}}(t_j)| / \max |\sigma_{N,\text{ex}}(t_j)| = 0.181 * 10^{-3}$  and  $\max |\sigma_{NT,\text{num}}(t_j) - \sigma_{NT,\text{ex}}(t_j)| / \max |\sigma_{NT,\text{ex}}(t_j)| = 0.283 * 10^{-3}$  at many discrete points (Fig. 2).

For the examination of the circumference stress component  $\sigma_T$  (Fig. 1), the following technique is suggested. In fact, in the plane strain case, the strain component  $\varepsilon_T$  (in T-direction) can be expressed as (Fig. 1)

$$\varepsilon_T = \frac{1}{E} (\sigma_T (1 - \nu^2) - \nu (1 + \nu) \sigma_N) \quad (20)$$

Considering  $\varepsilon_T$  and  $\sigma_N$  as two known values, from Eq. (20) we can evaluate  $\sigma_T$  by (Chen 2012b, 2012a)

$$\sigma_T = \frac{E \varepsilon_T + \nu (1 + \nu) \sigma_N}{1 - \nu^2} \quad (21)$$

where  $E$  is the Young's modulus of elasticity, and  $\nu$  is the Poisson's ratio (Chen 2012a).

In the Dirichlet problem, the component  $\sigma_N$  in Eq. (21) is obtained from the solution for  $Q(t)$  shown in Eq. (19). The strain component  $\varepsilon_T$  in the T-direction can be obtained from the given condition for  $U(t)$  (Chen 2012a).

In the Neumann problem, the component  $\sigma_N$  in Eq. (21) is given beforehand from the boundary condition. The strain component  $\varepsilon_T$  in the T-direction can be evaluated from the obtained solution for displacement on the boundary, or  $U(t)$  along the boundary (Chen 2012a).

In addition, the numerical solution  $\sigma_{T,\text{num}}(t)$  is compared with exact one. After computation, we find the following error  $\max |\sigma_{T,\text{num}}(t_j) - \sigma_{T,\text{ex}}(t_j)| / \max |\sigma_{T,\text{ex}}(t_j)| = 0.502 * 10^{-4}$  from many discrete points. From above mentioned results we see that the suggested technique provides a very accurate result in the example.

In addition, the stress components along the boundary  $\Gamma$  ( $x = a \cos \theta$ ,  $y = b \sin \theta$ ) are expressed by

$$\sigma_N = f_1(\theta)p, \quad \sigma_{NT} = f_2(\theta)p, \quad \sigma_T = f_3(\theta)p \quad (22)$$

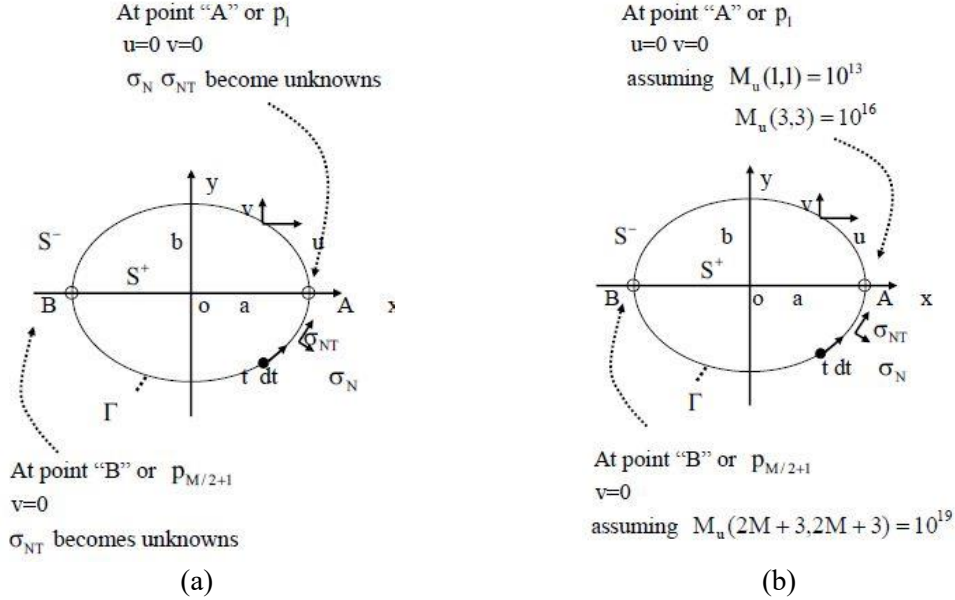


Fig. 3 Different techniques in the solution of Neumann problem for the interior region: (a) scheme of solution in the second technique, (b) scheme of solution in the third technique ( $M=48$  used in computation)

The exact and the computed results for  $f_1(\theta)$ ,  $f_2(\theta)$  and  $f_3(\theta)$  are plotted in Fig. 2. In Fig. 2, the solid line is derived from the exact solution, and the dashed line from the numerical solution. From the figure we see that the numerical solution provides very accurate result.

In the third examination, we study the Neumann problem. In the Neumann problem, the  $Q(t)$  component denoted by  $\{Q_{ex}(t)\}$  can be exactly evaluated beforehand, which is derived from the complex potentials shown by Eq. (13) with  $c_1 = 0.5 + 0.8i$  and  $c_2 = 1.1 + 0.6i$  directly.

Three techniques are suggested to solve the Neumann problem (Fig. 3).

In the first technique, from Eq. (14) we can get the solution for  $\{U_{num}(t)\}$  by

$$\{U_{num}(t)\} = \mathbf{M}_U^{-1} \mathbf{M}_Q \{Q_{ex}(t)\} \quad (t \text{ denoting the discrete points}) \quad (23)$$

where  $\mathbf{M}_U^{-1}$  denotes the inverse of the matrix  $\mathbf{M}_U$ . In the numerical solution, we have  $\det(\mathbf{M}_U) \approx 0$  and  $\det(\mathbf{M}_U) \neq 0$ . Thus, we can evaluate the matrix  $\mathbf{M}_U^{-1}$  accordingly.

As stated previously, we can evaluate the component  $\sigma_{T,num}(t)$ . The numerical solution  $\sigma_{T,num}(t)$  is compared with exact one. The computed results for  $\sigma_{T,num}(t)$  in the first technique is plotted in Fig. 4. In computation, we find the following error

$$\max |\sigma_{T,num}(t_j) - \sigma_{T,ex}(t_j)| / \max |\sigma_{T,ex}(t_j)| = 0.357 * 10^{-3}$$

from many discrete points. The computed results for  $\sigma_{T,num}(t)$  in the first technique is plotted in Fig. 4.

The second technique for the solution in the Neumann problem is suggested below (Fig. 3).

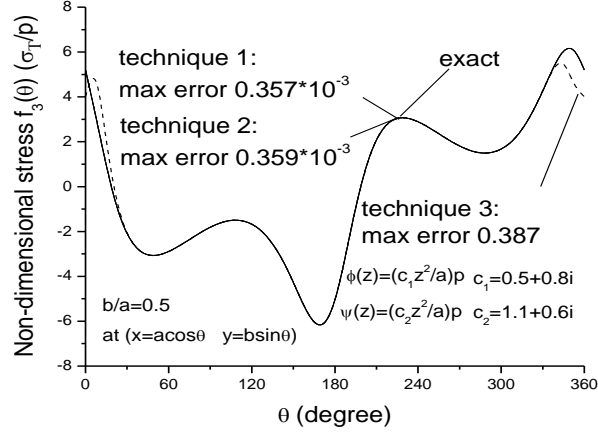


Fig. 4 Comparisons for three non-dimensional stresses  $f_3(\theta) = \sigma_T / p$  in a Neumann problem for an elliptic plate in the case of  $c_1 = 0.5 + 0.8i$ ,  $c_2 = 1.1 + 0.6i$ , and  $b/a=0.5$  by using different techniques (see Fig. 1, Eq. (13) and Appendix A)

In the Neumann problem for the interior region, three rigid motion modes may be involved in the solution for the displacement. In order to obtain a definite solution for the displacement, the second technique for the problem is suggested. In the second technique, we assumed that (a) at the point A ( $x=a, y=0$ ) in Fig. 3, or at the point  $p_1$ , we take  $u=0$  and  $v=0$ , (b) at the point B ( $x=-a, y=0$ ), or at the point  $p_{M/2+1}$ , we take  $v=0$ . In addition, we consider the problem as a mixed boundary value problem. That is to say at the point A ( $x=a, y=0$ ) two displacements  $u=0$  and  $v=0$  are two known values and two tractions  $\sigma_N$  and  $\sigma_{NT}$  become the unknowns. Similarly, at the point B ( $x=-a, y=0$ ) the displacements  $v=0$  is a known value and the traction  $\sigma_{NT}$  become the unknown. In the mixed BVP, we just move three columns from left side of Eq. (14) to right side, and relevant three columns from right side of Eq. (14) to left side. Since the second technique can model the physical situation very well, this technique provides most effective way in the solution of the Neumann problem.

In addition, the numerical solution  $\sigma_{T,num}(t)$  is compared with exact one. The computed results for  $\sigma_{T,num}(t)$  from the second technique is also plotted in Fig. 4. In computation, we find the following error  $\max |\sigma_{T,num}(t_j) - \sigma_{T,ex}(t_j)| / \max |\sigma_{T,ex}(t_j)| = 0.359 * 10^{-3}$  from many discrete points in the second technique.

The third technique for the solution in the Neumann problem is suggested below (Fig. 3). The assumptions used in the second technique, or (a) at the point A ( $x=a, y=0$ ), we take  $u=0$  and  $v=0$ , (b) at the point B ( $x=-a, y=0$ ), we take  $v=0$ , are still used in the present technique. However, in order to satisfy the mentioned conditions, we only assume that there elements in the diagonal in the matrix  $M_U$  take a huge value. In the  $M=48$  case, corresponding to the mentioned conditions we can let  $M_U(1,1) = 10^{13}$ ,  $M_U(3,3) = 10^{16}$ ,  $M_U(99,99) = 10^{19}$ . Physically, the stress field at the vicinity of points  $p_1$  and  $p_{M/2+1}$  has been seriously disturbed. Thus, the third technique cannot

provide an accurate result within the whole range ( $0 \leq \theta \leq 2\pi$ ) along the elliptic contour.

In addition, the numerical solution  $\sigma_{T,num}(t)$  is compared with exact one. The computed results for  $\sigma_{T,num}(t)$  in the third technique is also plotted in Fig. 4. After computation, we find the following error  $\max|\sigma_{T,num}(t_j) - \sigma_{T,ex}(t_j)| / \max|\sigma_{T,ex}(t_j)| = 0.387$  from many discrete points in the third technique. From Fig. 4, we see that in most range  $\pi/6 \leq \theta \leq 11\pi/6$  the computed results  $\sigma_{T,num}(t_j)$  coincide with the  $\sigma_{T,ex}(t_j)$  very well.

### 3. The Null Field CVBIE for an exterior region in plane elasticity

As studied in the second section, general formulation for the null field CVBIE for an exterior region is suggested. The same accurate shape function proposed in the second section is still used here in the discretization of BIE. Numerical examples are carried out

#### 3.1 General formulation for the null field CVBIE for an exterior region

Previously, a CVBIE for the exterior region was suggested (Chen 2012a). After dropping the free term in the usual CVBIE, and assuming the source point  $t_0$  to be inside the contour  $\Gamma$ , or  $t_0 \in S^+$  (Fig. 5), we have the following null field CVBIE for the exterior BVP (boundary value problem)

$$\begin{aligned} & 2G \int_{\Gamma} \left( \frac{\kappa-1}{t-t_0} U(t) dt - L_1(t, t_0) U(t) dt + L_2(t, t_0) \overline{U(t)} dt \right) \\ & = \int_{\Gamma} \left( 2\kappa \ln|t-t_0| Q(t) dt + \frac{t-t_0}{t-t_0} \overline{Q(t)} dt \right) (t_0 \in S^+, \text{ for exterior BVP}) \end{aligned} \quad (24)$$

It is worth pointing out that the left side terms in Eqs. (1) and (24) (in Eq. (1)  $t_0 \in S^-$ , and in Eq. (24)  $t_0 \in S^+$ ) have quite different property, even though they have same expression. If one evaluates the first term in the left hand of Eqs. (1) and (24), we will find the following results

$$\frac{1}{2\pi i} \int_{\Gamma} \frac{dt}{t-t_0} = 0, \quad (t_0 \in S^-) \quad (25)$$

$$\frac{1}{2\pi i} \int_{\Gamma} \frac{dt}{t-t_0} = 1, \quad (t_0 \in S^+) \quad (26)$$

From Eqs. (25) and (26), we will find a significant difference between two operators shown in left side of Eqs. (1) and (24).

In addition, if substituting  $Q(t)=0$  in Eqs. (1) and (24), we will obtain the following homogenous CVBIE

$$\int_{\Gamma} \left( \frac{\kappa-1}{t-t_0} U(t) dt - L_1(t, t_0) U(t) dt + L_2(t, t_0) \overline{U(t)} dt \right) = 0 \quad (t_0 \in S^-, \text{ for interior BVP}) \quad (27)$$

$$\int_{\Gamma} \left( \frac{\kappa-1}{t-t_0} U(t) dt - L_1(t, t_0) U(t) dt + L_2(t, t_0) \overline{U(t)} dt \right) = 0 \quad (t_0 \in S^+, \text{ for exterior BVP}) \quad (28)$$

We have numerically checked that the rigid mode motions along the boundary  $\Gamma$  are non-trivial solution for interior BVP shown by Eq. (27), or  $t_0 \in S^-$  for interior BVP. For the limitation of space, we do not show the detailed result. On contrary, for the homogeneous BIE shown by Eq. (28), or  $t_0 \in S^+$  for exterior BVP, we only have the trivial solution  $U(t)=0$  along the boundary  $\Gamma$ .

Similar to the interior BVP, we can use the same interpolation for the shape function, which is shown by Eqs. (7) and (8) (Fig. 5).

As mentioned above, after making discretization to Eq. (24), the BIE can be written in the form

$$\mathbf{M}_U \{U(t)\} = \mathbf{M}_Q \{Q(t)\} \quad (t \text{ denoting the discrete points}) \quad (29)$$

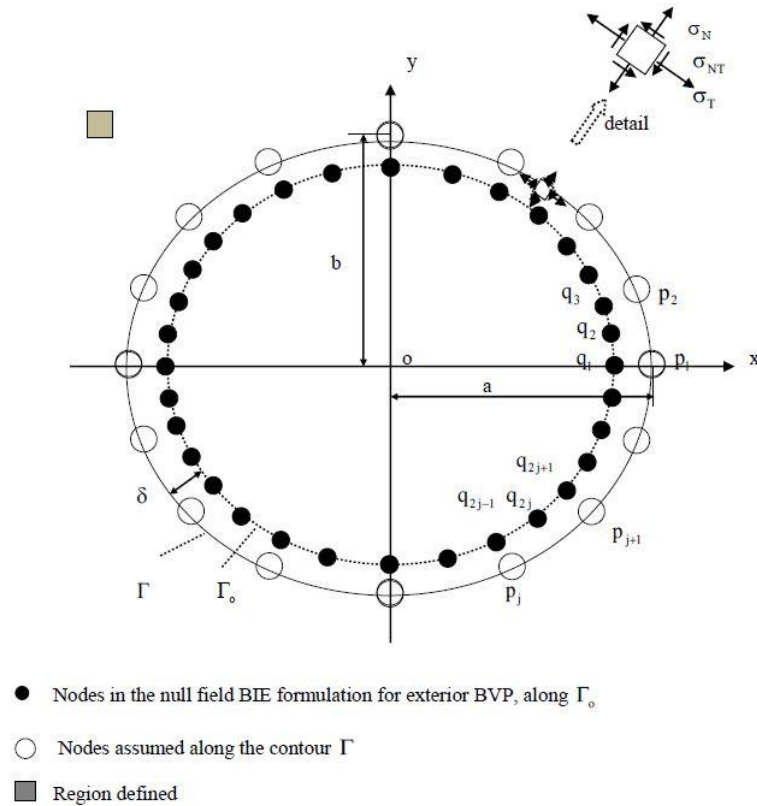


Fig. 5 Formulation of the null field CVBIE for an exterior region

where  $\mathbf{M}_U$  is a matrix acting upon the displacement vector  $\{U(t)\}$ , and  $\mathbf{M}_Q$  is a matrix acting upon the traction vector  $\{Q(t)\}$ . Even though the form of matrix  $\mathbf{M}_U$  in the exterior BVP is same as the form for the matrix in the interior BVP which is obtained in the second section, the two matrices have significant difference. In the  $\mathbf{M}_U \{U(t)\}$  expression for the interior BVP, the source point  $t_o$  is located outside of the elliptic contour  $\Gamma$  (Fig. 1). However, in the  $\mathbf{M}_U \{U(t)\}$  expression for the exterior BVP, the source point  $t_o$  is located inside of the elliptic contour  $\Gamma$  (Fig. 5). Clearly, the inverse matrix  $\mathbf{M}_U^{-1}$  exists in the exterior BVP.

### 3.2 Numerical examples

Two numerical examples are provided to prove that the higher accuracy has been achieved in the suggested technique. Particularly, in the second example, the influences caused by (a) the scale of discretization, (b) the location of the null field nodes and (3) the type of the BVP are carefully examined.

In the first example, we study the exterior BVP with the elliptic contour  $\Gamma$  (Fig. 5). The same computation conditions used in second section are used in the present example. The ellipse for null field nodes  $t_o$  is defined by  $x = (a - \delta)\cos\theta$ ,  $y = (b - \delta)\sin\theta$ . or  $t_o \in \Gamma_o$  (Fig. 5). and  $\delta = 0.02a$  is used in computation.

In the present example, we use the following complex potentials

$$\phi(z) = -\frac{P}{2\pi(\kappa+1)} \ln z, \quad \psi(z) = \frac{\kappa P}{2\pi(\kappa+1)} \ln z \quad (30)$$

where ‘‘P’’ is a loading, which corresponds a concentrated force acted at the origin.

From Eq. (30), we can evaluate the relevant displacements and stresses by using the Appendix A. In addition, we choose  $a=20$ ,  $b=10$  and  $G=2$  in computation

As mentioned above, after discretization to Eq. (24), the BIE can be written in the form

$$\mathbf{M}_U \{U(t)\} = \mathbf{M}_Q \{Q(t)\} \quad (t \text{ denoting the discrete points}) \quad (31)$$

where  $\mathbf{M}_U$  is a matrix acting upon the displacement vector  $\{U(t)\}$ , and  $\mathbf{M}_Q$  is a matrix acting upon the traction vector  $\{Q(t)\}$ .

In the first examination, we will check the approximate behavior for the left hand and the right hand term of Eq. (31). From Eq. (31), we can evaluate the relevant displacements and stresses by using the Appendix A.

As stated before in second section, we can define a vector

$$\{e_1(t_o)\} = \{U_p(t_o)\} - \{Q_p(t_o)\} = \mathbf{M}_U \{U_{ex}(t)\} - \mathbf{M}_Q \{Q_{ex}(t)\} \quad (t_o \in \Gamma_o) \quad (32)$$

and define an error estimation value

$$\frac{\max \{|e_1(t_o)|\}}{\max \text{ of } |\mathbf{M}_U \{U_{ex}(t_o)\}| \text{ and } |\mathbf{M}_Q \{Q_{ex}(t_o)\}|} \quad (33)$$

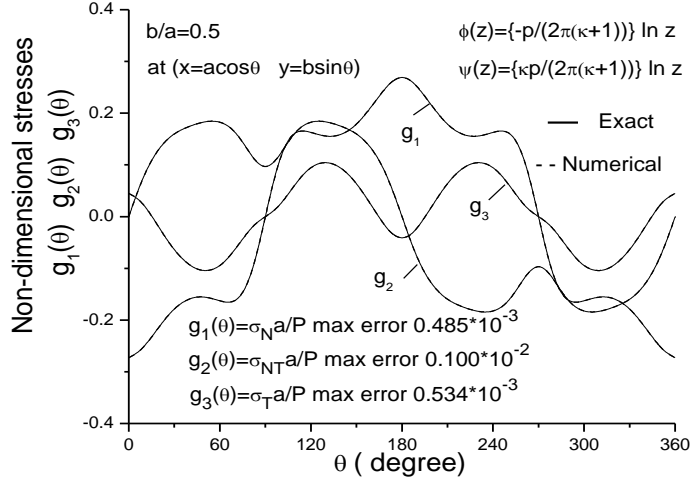


Fig. 6 Three non-dimensional stresses  $g_1(\theta) = \sigma_N a/P$ ,  $g_2(\theta) = \sigma_{NT} a/P$ ,  $g_3(\theta) = \sigma_T a/P$  in a Dirichlet problem for an elliptic plate (see Fig. 5 and Eq. (35))

After computation, we find the following error  $\mathbf{E}_{r1} = 0.701 * 10^{-5}$  from 2M discrete points. Clearly, the error is very small.

In the second examination, we study the Dirichlet problem. In the Dirichlet problem, the  $U(t)$  component denoted by  $\{U_{ex}(t)\}$  can be exactly evaluated beforehand, which is from the complex potentials shown by Eq. (30).

Thus, from Eq. (24), we can get the solution for  $\{Q_{num}(t)\}$  by

$$\{Q_{num}(t)\} = \mathbf{M}_Q^{-1} \mathbf{M}_U \{U_{ex}(t)\}, \quad (t \text{ denoting the discrete points}) \quad (34)$$

In addition, the stress components along the boundary ( $x = a \cos \theta$ ,  $y = b \sin \theta$ ) are expressed by

$$\sigma_N = g_1(\theta) \frac{P}{a}, \quad \sigma_{NT} = g_2(\theta) \frac{P}{a}, \quad \sigma_T = g_3(\theta) \frac{P}{a} \quad (35)$$

The exact and the computed results for  $g_1(\theta)$ ,  $g_2(\theta)$  and  $g_3(\theta)$  are plotted in Fig. 6. In the figure, the solid line is derived from the exact solution, and the dashed line from the numerical solution. From the figure we see that the numerical solution provides very accurate result.

In addition, we can find the following error estimation:

$$\begin{aligned} \max |\sigma_{N,num}(t_j) - \sigma_{N,ex}(t_j)| / \max |\sigma_{N,ex}(t_j)| &= 0.485 * 10^{-3}, \\ \max |\sigma_{NT,num}(t_j) - \sigma_{NT,ex}(t_j)| / \max |\sigma_{NT,ex}(t_j)| &= 0.100 * 10^{-2} \quad \text{and} \\ \max |\sigma_{T,num}(t_j) - \sigma_{T,ex}(t_j)| / \max |\sigma_{T,ex}(t_j)| &= 0.534 * 10^{-3} \quad \text{at many discrete points. Clearly, the} \end{aligned}$$

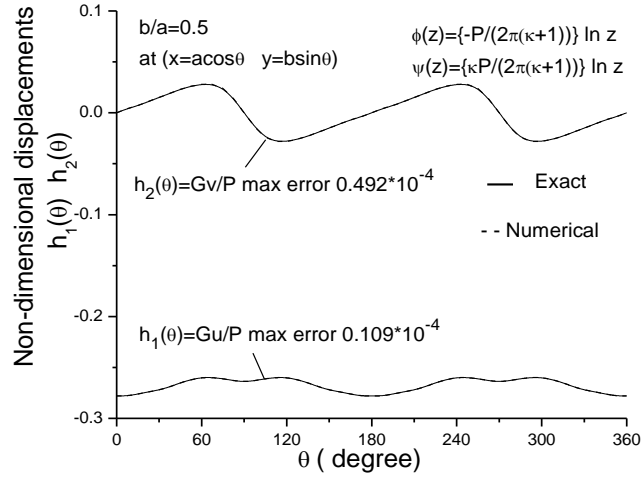


Fig. 7 Two non-dimensional displacements  $h_1(\theta) = Gu/P$ ,  $h_2(\theta) = Gv/P$ , in a Neumann problem of the exterior BVP for an elliptic plate (see Fig. 5 and Eq. (37))

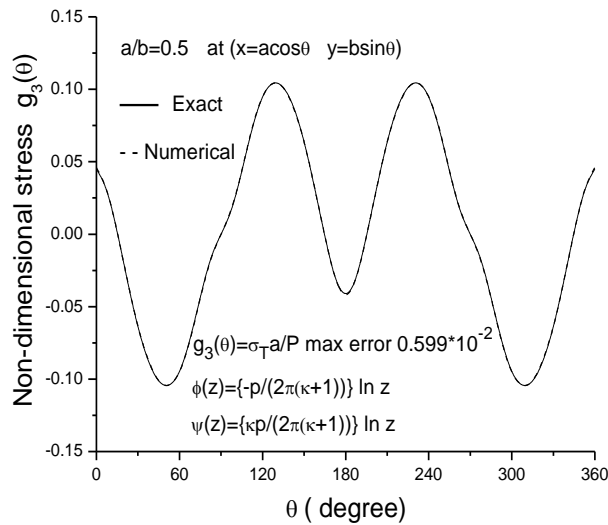


Fig. 8 The non-dimensional stress  $g_3(\theta) = \sigma_T a/P$  in a Neumann problem of the exterior BVP for an elliptic plate (see Fig. 5 and Eq. (37))

error is very small.

In the third examination, we study the Neumann problem. In the Neumann problem, the  $Q(t)$  component denoted by  $\{Q_{ex}(t)\}$  can be exactly evaluated beforehand, which is from the complex potentials shown by Eq. (30).

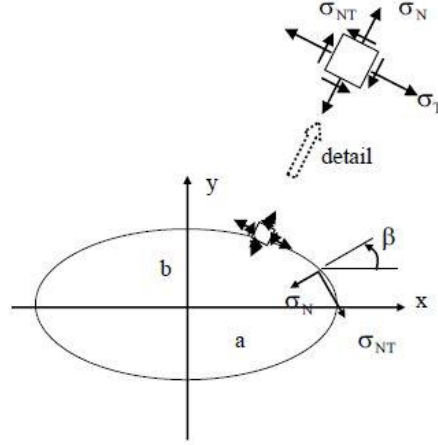


Fig. 9 An elliptic notch in an infinite plate with loading applied on the contour

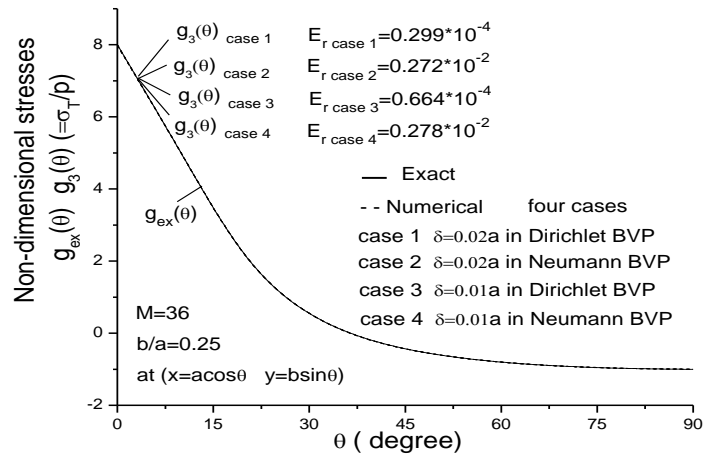


Fig. 10 Non-dimensional stresses  $g_{ex}(\theta)$ ,  $g_3(\theta)$  ( $=\sigma_T/p$ ) for four cases at the point  $x = a \cos\theta$ ,  $y = b \sin\theta$  in the case of  $M=36$  (see Figs. 5 and 9).

Thus, from Eq. (31), we can get the solution for  $\{U_{num}(t)\}$  by

$$\{U_{num}(t)\} = \mathbf{M}_U^{-1} \mathbf{M}_Q \{Q_{ex}(t)\}, \quad (t \text{ denoting the discrete points}) \quad (36)$$

In addition, the computed displacement and the stress components along the boundary ( $x = a \cos\theta$ ,  $y = b \sin\theta$ ) are expressed by

$$\mathbf{u} = h_1(\theta) \frac{P}{G}, \quad v = h_2(\theta) \frac{P}{G}, \quad \sigma_T = g_3(\theta) \frac{P}{a} \quad (37)$$

Table 1 Non-dimensional stresses  $g_{ex}(\theta)$ ,  $g_3(\theta)(=\sigma_T/p)$  for four cases at the point  $x=acos \theta$ ,  $y=bcos \theta$  in the case of M-36 (see Figs. 5 and 9)

$\theta$ (deg)	0	10	20	30	40	50	60	70	80	90
$g_{ex}(\theta)$	8.000	5.010	1.885	0.421	-0.266	-0.621	-0.816	-0.926	-0.983	-1.000
$g_3(\theta)$ *1	8.000	5.010	1.885	0.421	-0.266	-0.621	-0.816	-0.926	-0.983	-1.000
$g_3(\theta)$ *2	7.978	5.022	1.885	0.420	-0.267	-0.621	-0.817	-0.926	-0.983	-1.000
$g_3(\theta)$ *3	8.000	5.010	1.885	0.421	-0.266	-0.621	-0.816	-0.927	-0.983	-0.999
$g_3(\theta)$ *4	7.978	5.023	1.886	0.420	-0.267	-0.621	-0.816	-0.928	-0.983	-0.998

\*1  $\delta = 0.02a$  in Dirichlet BVP      \*2  $\delta = 0.02a$  in Neumann BVP  
 \*3  $\delta = 0.01a$  in Dirichlet BVP      \*4  $\delta = 0.01a$  in Neumann BVP

The exact and the computed results for  $h_1(\theta)$ ,  $h_2(\theta)$  and  $g_3(\theta)$  are plotted in Figs. 7 and 8. In the figure, the solid line is derived from the exact solution, and the dashed line from the numerical solution. From the figure we see that the numerical solution provides very accurate result.

In addition, we can find the following error estimation:  $\max |u_{num}(t_j) - u_{ex}(t_j)| / \max |u_{ex}(t_j)| = 0.109 * 10^{-4}$ ,  $\max |v_{num}(t_j) - v_{ex}(t_j)| / \max |v_{ex}(t_j)| = 0.493 * 10^{-4}$  and  $\max |\sigma_{T,num}(t_j) - \sigma_{T,ex}(t_j)| / \max |\sigma_{T,ex}(t_j)| = 0.599 * 10^{-2}$  at many discrete points. Clearly, the error is very small.

In the second example, we check the accuracy archived in the suggested method. In the example, it is assumed that at the boundary point  $x = \cos \theta$   $y = b \sin \theta$  the following loading is applied (Fig. 9)

$$\sigma_N = -p \sin^2 \beta, \quad \sigma_{NT} = -p \sin \beta \cos \beta \quad (\text{with } \beta = \text{Arc tan } \frac{a \sin \theta}{b \cos \theta}) \quad (38)$$

After using the following conformal mapping (Muskhelishvili 1953)

$$z = \omega(\zeta) = R(\zeta + \frac{m}{\zeta}), \quad (\text{with } R = \frac{a+b}{2}, \quad m = \frac{a-b}{a+b}) \quad (39)$$

We can obtain the following complex potentials (Muskhelishvili 1953)

$$\phi(\zeta) = -\frac{(1+m)Rp}{2} \frac{1}{\zeta} \quad (40)$$

$$\psi(\zeta) = -\frac{(1+m)^2 Rp}{2} \frac{1}{\zeta} - \frac{(1+m)(1+m)^2 Rp}{2} \frac{1}{\zeta(\zeta^2 - m)} \quad (41)$$

If we assume the displacements along the boundary from the complex potentials shown by Eqs. (40) and (41), the Dirichlet BVP (boundary value problem) is formulated. Therefore, the tractions

along the boundary will be obtained from the null field BIE shown by Eq. (24). Similarly, if we assume the tractions along the boundary from the complex potentials shown by Eqs. (40) and (41), the Neumann BVP is formulated. In addition, the displacements along the boundary will be obtained from the BIE shown by Eq. (24).

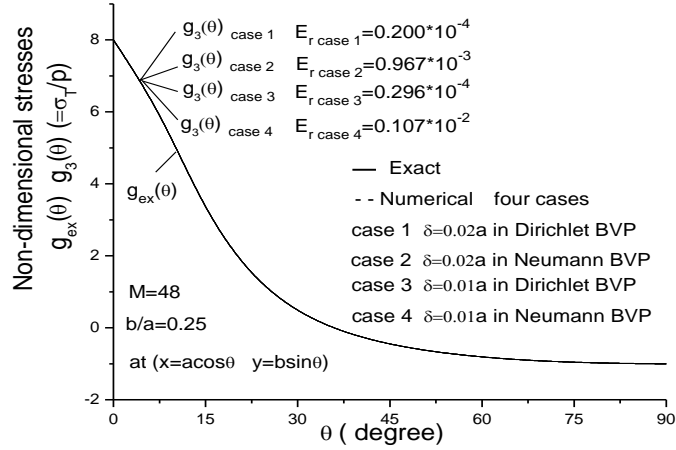


Fig. 11 Non-dimensional stresses  $g_{ex}(\theta)$ ,  $g_3(\theta)$  ( $=\sigma_T/p$ ) for four cases at the point  $x = a \cos \theta$ ,  $y = b \sin \theta$  in the case of  $M=48$  (see Figs. 5 and 9)

Table 2 Non-dimensional stresses  $g_{ex}(\theta)$ ,  $g_3(\theta)$  ( $=\sigma_T/p$ ) for four cases at the point  $x=a\cos\theta$ ,  $y=b\sin\theta$  in the case of  $M=48$  (see Figs 5 and 9)

$\theta$ (deg)	0	15	30	45	60	75	90
$g_{ex}(\theta)$	8.000	3.188	0.421	-0.471	-0.816	-0.960	-1.000
$g_3(\theta)$ *1	8.000	3.188	0.421	-0.471	-0.816	-0.960	-1.000
$g_3(\theta)$ *2	7.992	3.190	0.421	-0.471	-0.816	-0.960	-1.000
$g_3(\theta)$ *3	8.000	3.188	0.421	-0.471	-0.816	-0.960	-1.000
$g_3(\theta)$ *4	7.991	3.190	0.420	-0.471	-0.816	-0.960	-1.000

\*1  $\delta = 0.02a$  in Dirichlet BVP      \*2  $\delta = 0.02a$  in Neumann BVP

\*3  $\delta = 0.01a$  in Dirichlet BVP      \*4  $\delta = 0.01a$  in Neumann BVP

As before, the computed stress component  $\sigma_T$  along the boundary ( $x = a \cos \theta$ ,  $y = b \sin \theta$ ) is expressed by

$$\sigma_T = g_3(\theta)p \quad (42)$$

In the meantime, the exact solution derived from the complex potentials shown by Eqs. (40) and (41) is expressed by

$$\sigma_T = g_{ex}(\theta)p \quad (43)$$

We can define an error estimation value as follows

$$E_r = \frac{\max |g_{ex}(\theta) - g_3(\theta)|}{\max |g_{ex}(\theta)|} \quad (44)$$

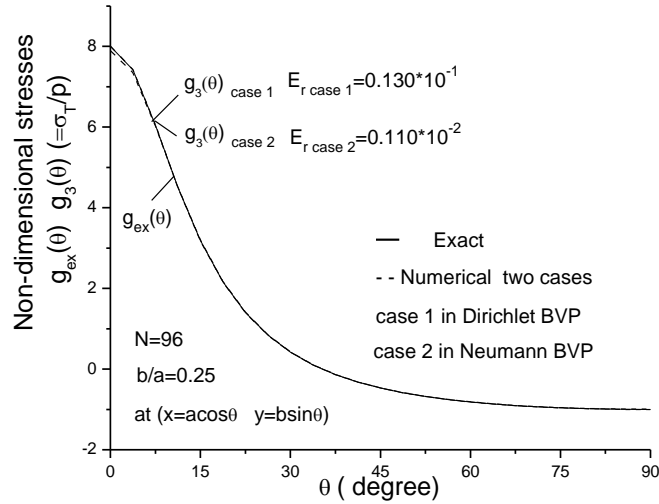


Fig. 12 Non-dimensional stresses,  $g_{ex}(\theta)$ ,  $g_3(\theta)(=\sigma_T/p)$  for two cases at the point  $x=acos\theta$ ,  $y=bcos\theta$  in the case of using usual BIE (Chen 2012a) ( see Fig. 9)

Table 3 Non-dimensional stresses  $g_{ex}(\theta)$ ,  $g_3(\theta)(=\sigma_T/p)$  for four cases at the point  $x=acos\theta$ ,  $y=bcos\theta$  in the case of using usual BIE (Chen 2012a, see Fig. 9)

$\theta$ (deg)	0.	15	30	45	60	75	90
$g_{ex}(\theta)$	8.000	3.188	0.421	-0.471	-0.816	-0.960	-1.000
$g_3(\theta) *1$	7.896	3.201	0.426	-0.470	-0.818	-0.962	-1.002
$g_3(\theta) *2$	8.009	3.180	0.419	-0.468	-0.811	-0.953	-0.993

\*1 in Dirichlet BVP      \*2 in Neumann BVP

In fact, the error estimation defined by  $E_r$  depends on three factors (a) the number of division used along the boundary  $\Gamma$ , or the number  $M$  in Eqs. (11) and (12), (b) the locations of nodes used in the computation, or the value for  $\delta$  assumed in the computation (see Fig. 5) and (c) the type of the BVP used, or the Dirichlet BVP and the Neumann BVP in the formulation.

In the condition of (a)  $\delta = 0.02a$  or  $\delta = 0.01a$  and (b) the Dirichlet problem or the Neumann problem in the formulation, we can define the following four error estimation values

In the following analysis, we propose three groups for computation. In all cases, we choose  $b/a=0.25$ .

In the first group computation, we choose  $M=36$  and use the null field BIE Shown by Eq. (24).

For the mentioned four cases, the computed  $g_{ex}(\theta)$ ,  $g_3(\theta)$  (four cases) are plotted in Fig. 10 and

Table 1. In addition, the computed error estimation values are also listed in Fig. 10.

In the numerical computation, we provide four kinds of variation, or (1) case-1,  $\delta = 0.02a$  in Dirichlet BVP, (2) case-2,  $\delta = 0.02a$  in Neumann BVP, (3) case-3,  $\delta = 0.01a$  in Dirichlet BVP and (4) case-4,  $\delta = 0.01a$  in Neumann BVP. The results for  $g_{ex}(\theta) = \sigma_T/p$  and the computed results for the non-dimensional stresses  $g_3(\theta) (\sigma_T/p)$  for four cases at the point  $x = a \cos \theta$ ,  $y = b \cos \theta$  in the case of  $M=36$  (see Eqs. (11) and (12)) are plotted in Fig. 10. From Fig. 10 we see that, the computed results for  $g_{ex}(\theta)$  (with solid line) and  $g_3(\theta)$  (four cases with dashed lines) are merged into one curve. In all four cases, the  $E_r$  values generally take a rather small value. For example, in the case-2 (or  $\delta = 0.02a$  in Neumann BVP), we have  $E_{r \text{ case-2}} = 0.272 * 10^{-2}$  (or 0.00272) (see Fig. 10). This is a very small value.

From Table 1 we see that at  $\theta = 0^\circ$  we have  $g_{ex}(\theta) |_{\theta=0^\circ} = 8.000$  and  $g_3(\theta) |_{\theta=0^\circ \text{ case-2}} = 7.978$  and  $g_3(\theta) |_{\theta=0^\circ \text{ case-4}} = 7.978$ . Note that, the case-2 and the case-4 correspond to  $\delta = 0.02a$  and  $\delta = 0.01a$ , respectively. Thus, both the options  $\delta = 0.02a$  and  $\delta = 0.01a$  provide an accurate result.

In the second group computation, we choose  $M=48$  and use the null field BIE (24).

For the mentioned four cases, the computed  $g_{ex}(\theta)$  and  $g_3(\theta)$  (four cases) are plotted in Fig. 11 and Table 2. In addition, the computed error estimation values are also listed in Fig. 11.

From a comparison between Figs. 10 and 11, we find the following result. In the case of  $M=36$ , we have  $E_{r \text{ case-1}} = 0.299 * 10^{-4}$ ,  $E_{r \text{ case-2}} = 0.272 * 10^{-2}$ ,  $E_{r \text{ case-3}} = 0.664 * 10^{-4}$  and  $E_{r \text{ case-4}} = 0.278 * 10^{-2}$ . In the case of  $M=48$ , we have  $E_{r \text{ case-1}} = 0.200 * 10^{-4}$ ,  $E_{r \text{ case-2}} = 0.967 * 10^{-3}$ ,  $E_{r \text{ case-3}} = 0.296 * 10^{-4}$  and  $E_{r \text{ case-4}} = 0.107 * 10^{-2}$ . That is to say, if the number of divisions along the boundary is changed from  $M=36$  to  $M=48$ , a more accurate result will be obtained.

In the third group computation, we choose  $N=96$  and use the usual BIE (Chen 2012a).  $N=96$  is the number of divisions used in the usual BIE. In addition,  $N=98$  corresponds  $M=48$  used in the second group computation for the null field BIE.

Under the same geometry and loading conditions, for the two cases, the computed  $g_{ex}(\theta)$  and  $g_3(\theta) (= \sigma_T/p)$  (two cases) are plotted in Fig. 12 and Table 3. In addition, the computed error estimation values are also listed in Fig. 12.

From a comparison between Figs. 11 and 12, we find the following result. For example, in the null field BIE formulation with  $M=48$  (see Fig. 11), we have  $E_{r \text{ case-1}} = 0.200 * 10^{-4}$ ,  $E_{r \text{ case-2}} = 0.967 * 10^{-3}$ . However, in the usual BIE formulation with  $N=96$  (see Fig. 12), we have  $E_{r \text{ case-1}} = 0.130 * 10^{-1}$ ,  $E_{r \text{ case-2}} = 0.110 * 10^{-2}$ . Therefore, we can conclude that the accuracy achieved in the usual BIE is worse than that achieved in the null field formulation.

#### 4. Conclusions

This paper provides a numerical solution for null field CVBIE in plane elasticity. In the formulation, an accurate shape function along the contour is suggested. The suggested shape

function belongs to the  $C^1$  continuity. Since the suggested shape function has a higher accuracy, the errors in numerical examples generally take a very small value, for example, less than one percentage.

In order to obtain a definite displacement in the Neumann problem for interior BVP, the best way is to reduce the interior BVP into a mixed BVP for the interior region.

## References

- Brebbia, C.A., Telles, J.C.F. and Wrobel, L.C. (1984), *Boundary Element Techniques - Theory and Applications in Engineering*, Springer, Heidelberg
- Chen, J.T. and Lee, Y.T. (2009), "Torsional rigidity of a circular bar with multiple circular inclusions using the null-field integral approach", *Comput. Mech.*, **44**, 221-232. <https://doi.org/10.1007/s00466-009-0365-8>.
- Chen, J.T. and Wu, A.C. (2007), "Null-field approach for the multi-inclusion problem under antiplane shears", *J. Appl. Mech.*, **74**, 469-487. <https://doi.org/10.1115/1.2338056>.
- Chen, J.T., Kuo, S.R. and Lin, J.H. (2002), "Analytical study and numerical experiments for degenerate scale problems in the boundary element method for two-dimensional elasticity", *Int. J. Numer. Meth. Eng.*, **54**, 1669-1681. <https://doi.org/10.1002/nme.476>.
- Chen, Y.Z. (2012a), "Boundary integral equation method for two dissimilar elastic inclusions in an infinite plate", *Eng. Anal. Bound. Elem.*, **36**(2), 137-146. <https://doi.org/10.1016/j.enganabound.2011.07.006>.
- Chen, Y.Z. (2012b), "An iteration approach for multiple notch problem based on complex variable boundary integral equation", *Struct. Eng. Mech.*, **41**(5), 591-604. <http://dx.doi.org/10.12989/sem.2012.41.5.591>.
- Chen, Y.Z. and Wang, Z.X. (2013), "Properties of integral operators in complex variable boundary integral equation in plane elasticity", *Struct. Eng. Mech.*, **45**(4), 495-519. <http://dx.doi.org/10.12989/sem.2013.45.4.495>.
- Chen, Y.Z., Lin, X.Y. and Wang, Z.X. (2010), "Formulation of indirect BIEs in plane elasticity using single or double layer potentials and complex variable"; *Eng. Anal. Bound. Elem.*, **34**, 337-351. <https://doi.org/10.1016/j.enganabound.2009.10.009>.
- Cheng, A.H.D. and Cheng, D.S. (2005), "Heritage and early history of the boundary element method", *Eng. Anal. Bound. Elem.*, **29**(3), 286-302. <https://doi.org/10.1016/j.enganabound.2004.12.001>.
- Cruse, T.A. (1969), "Numerical solutions in three-dimensional elastostatics", *Int. J. Solids Struct.*, **5**(12), 1259-1274. [https://doi.org/10.1016/0020-7683\(69\)90071-7](https://doi.org/10.1016/0020-7683(69)90071-7).
- Hildebrand, F.B. (1974), *Introduction to numerical analysis*, McGraw-Hill, New York.
- Hong, H.K. and Chen, J.T. (1988), "Derivations of integral equations of elasticity", *J. Eng. Mech.*, **114**(6), 1028-1044. [https://doi.org/10.1061/\(ASCE\)0733-9399\(1988\)114:6\(1028\)](https://doi.org/10.1061/(ASCE)0733-9399(1988)114:6(1028)).
- Jaswon, M.A. and Symm, G.T. (1977), *Integral Equation Methods in Potential Theory and Elastostatics*, Academic Press, London.
- Liu, Y.J. and Rudolphi, T.J. (1999), "New identities for fundamental solutions and their applications to non-singular boundary element formulation", *Comput. Mech.*, **24**, 286-292.
- Liu, Y.J., Ye, W. and Deng, Y. (2013), "On the identities for electrostatic fundamental solution and nonuniqueness of the traction BIE solution for multiconnected domains", *J. Appl. Mech.*, **80**(5), 051012-1 to -9. <https://doi.org/10.1115/1.4023640>.
- Muskhelishvili, N.I. (1953), *Some Basic Problems of the Mathematical Theory of Elasticity*, Noordhoff, The Netherlands.
- Rizzo, F.J. (1967), "An integral equation approach to boundary value problems in classical elastostatics", *Quart. J. Appl. Math.*, **25**, 83-95.
- Vodicka, R. and Mantic, V. (2008), "On solvability of a boundary integral equation of the first kind for Dirichlet boundary value problems in plane elasticity", *Comput. Mech.*, **41**(6), 817-826.

<https://doi.org/10.1007/s00466-007-0202-x>.

Zhang, X.S. and Zhang X.X. (2008), "Exact solution for the hypersingular boundary integral equation of two-dimensional elastostatics", *Struct. Eng. Mech.*, **30**(3), 279-296.

TK

### Appendix: A Some preliminary knowledge in complex variable method in plane elasticity

The complex variable function method plays an important role in plane elasticity. Fundamental of this method is introduced. In the method, the stresses ( $\sigma_x, \sigma_y, \sigma_{xy}$ ), the resultant forces ( $X, Y$ ) and the displacements ( $u, v$ ) are expressed in terms of complex potentials  $\phi(z)$  and  $\psi(z)$  such that (Muskhelishvili 1953)

$$\sigma_x + \sigma_y = 4\text{Re } \phi'(z), \quad \sigma_y - \sigma_x + 2i\sigma_{xy} = 2[\bar{z}\phi''(z) + \psi'(z)], \quad \sigma_y - \sigma_x - 2i\sigma_{xy} = 2[z\overline{\phi''(z)} + \overline{\psi'(z)}] \quad (\text{a1})$$

$$f = -Y + iX = \phi(z) + z\overline{\phi'(z)} + \overline{\psi(z)} \quad (\text{a2})$$

$$2G(u + iv) = \kappa\phi(z) - z\overline{\phi'(z)} - \overline{\psi(z)} \quad (\text{a3})$$

where a bar over a function denotes the conjugated value for the function,  $G$  is the shear modulus of elasticity,  $\kappa = (3 - \nu)/(1 + \nu)$  in the plane stress problem,  $\kappa = 3 - 4\nu$  in the plane strain problem, and  $\nu$  is the Poisson's ratio. Sometimes, the displacements  $u$  and  $v$  are denoted by  $u_1$  and  $u_2$ , the stresses  $\sigma_x, \sigma_y$  and  $\sigma_{xy}$  by  $\sigma_1, \sigma_2$  and  $\sigma_{12}$ , the coordinates  $x$  and  $y$  by  $x_1$  and  $x_2$ .